# A ReaxFF reactive force field for exploring electronically switchable polarization in $Zn_{1-x}Mg_xO$ ferroelectric semiconductors

Alireza Sepehrinezhad (abs6561@psu.edu)<sup>a</sup>, Steven M. Baksa (smb6448@psu.edu)<sup>b</sup>, Ismaila Dabo (ixd4@psu.edu)<sup>c</sup>, Adri C.T. van Duin (acv13@psu.edu)<sup>d, b, a, \*</sup>

Abstract – Cation misfit in traditional ferroelectric crystals offers a new material platform that can drive electronic components toward structural miniaturization and high-density integration, enabling deviation from von-Neumann architectures. Here, we explore ferroelectricity in Zn<sub>1</sub>- $_x$ Mg $_x$ O, a non-traditional ferroelectric material with tunable properties. Using data from densityfunctional theory calculations, we have developed a ReaxFF Reactive Force Field to explore ferroelectric properties of Zn<sub>1-x</sub>Mg<sub>x</sub>O and reveal the hysteresis behavior. We discover that ferroelectric switching is observable at a critical thickness of 10 nm with a remanent polarization of ~100 μC/cm<sup>2</sup>. Our analysis indicates that an increase in Mg-substitution correlates with a decrease in the coercive field. We also observe a strong temperature-dependence of the coercive field in Zn<sub>1-x</sub>Mg<sub>x</sub>O, with values decreasing as temperature increases. Additionally, we find that the distribution of Mg atoms significantly impacts the coercive field, with a clustered distribution leading to a substantial increase. In particular, a decrease in coercive field values is observed when Mg atoms are randomly distributed, compared to a uniform distribution. Leveraging tunable hysteresis behavior offered by varied percentage and distribution of Mg-substitution provides valuable insights into the design of next-generation functional devices and will inspire further investigations.

<sup>&</sup>lt;sup>a</sup> Department of Engineering Science and Mechanics, The Pennsylvania State University, University Park, PA, 16802, USA

<sup>&</sup>lt;sup>b</sup> Materials Research Institute, Department of Materials Science and Engineering, The Pennsylvania State University, University Park, PA, 16802, USA

<sup>&</sup>lt;sup>c</sup>Department of Materials Science and Engineering, and Wilton E. Scott Institute for Energy Innovation, Carnegie Mellon University, Pittsburgh, Pennsylvania 15213, USA

<sup>&</sup>lt;sup>d</sup> Department of Mechanical Engineering, The Pennsylvania State University, University Park PA 16802, USA

<sup>\*</sup>Corresponding author: acv13@psu.edu, Tel: 814-863-6277

Keywords – ReaxFF reactive force field, Ferroelectric materials, ZnMgO, Cation misfit.

#### 1 Introduction

Ferroelectric materials have emerged as a pivotal component in the realm of microelectronic devices, owing to their unique properties including robust spontaneous polarization, piezoelectric and pyroelectric effects, and large dielectric constants: a dielectric constant of 3400 has been reported for lead zirconate titanate (PZT, PbZr<sub>x</sub>Ti<sub>1-x</sub>O<sub>3</sub> where 0 < x < 1) [1] and a constant of 6000 reported for BaTiO<sub>3</sub> [2], to name but a few. These materials have been used in nonvolatile memories [3-6], transducers [7], capacitors [8], and photovoltaic devices [9].

Conventional perovskite ferroelectrics face limitations such as incompatible windows for synthesis and difficulties with scaling to dimensions below desired dimensions [10, 11]. These limitations have encouraged research beyond the traditional perovskite palette; relaxor ferroelectrics (RFs) have been studied for energy storage applications [12-14] to compensate for the high dielectric constant and loss, as well as large residual polarization of traditional ferroelectrics such as BaTiO<sub>3</sub> [8]. Doping perovskite ferroelectrics has been identified as an efficient way to improve and modify their properties [15-18]. For instance, Ce-doped BaTiO<sub>3</sub> achieves an increased dielectric permittivity as well as decreased Curie temperature, compared to its predecessor [19]. La- and Zr-doped BaTiO<sub>3</sub> obtains an increased dielectric permittivity [20]. Experimental studies have also shown that doping Fe or Mn into BaTiO<sub>3</sub> promotes polarization reversal [21-23].

While the above-mentioned studies investigate the tunability and modification of currently established ferroelectric materials, other studies have also shown the possibility of triggering ferroelectricity in a conventionally non-ferroelectric material through introduction of a chemical stressor or disorder. Early studies have shown that by applying a combination of preparation and formulation to a structurally simple crystal, one could, in principle, trigger ferroelectricity [24-26]. Consequently, recent studies on the use of dopants attract a more focused investigation on development of novel ferroelectric materials; It has been found that factors including strain, grain size, and defect chemistry can stabilize a switchable polar phase in HfO<sub>2</sub> [27], while the same could be accomplished for wurtzite AlN, by substituting ~20% Sc for Al [28]. These studies inspire the exploration of new ferroelectrics by proposing that any polar crystal has the potential to serve as a ferroelectric host, given the use of an appropriate dopant to enable the reorientation

of the crystal's polar axes. This paper explores the effect of cation misfit on the polarization reversal in the ZnO-MgO system.

ZnO is a II-VI wurtzite (space group P63mc) semiconductor with a spontaneous polarization of 90  $\mu$ C/cm<sup>2</sup> along the [0001] direction, a 3.4eV bandgap, a large excition binding energy of 60 meV, and a notable transparency [29]. It has lattice constants 3.25(5) and 5.21(8) Å at ambient conditions [30] and a bulk modulus of 140 GPa. It has a diverse range of applications in optoelectronics, solar cells, light emitting devices, and transparent electrodes [31-40]. Mg has been used as dopant to engineer the bandgap of ZnO and achieve a widegap semiconductor alloy, suitable for the fabrication of light emitting devices. It is shown that for a Mg content of 33%, a bandgap of up to  $\sim$ 4 eV can be achieved [41]. An increase in the exciton binding energy has also been observed for Zn<sub>1-x</sub>Mg<sub>x</sub>O alloys [42]. For high percentages of Mg, however, phase separation occurs after which MgO assumes a centrosymmetric structure, unlike ZnO which strongly favors the wurtzite structure. The solubility of MgO in a wurtzite solid solution has been found to be more than 40 mol% [41, 43-46].

ZnO was conventionally considered as non-ferroelectric; Because of its large coercive field and relatively low bandgap, dielectric breakdown happens before the polarization reversal is initiated. In other words, the leakage current in ZnO is so large that prohibits the switching, although in the case of a biaxially strained ZnO, ferroelectricity has been demonstrated by computation and experiment [29, 47]. Solubility and wide bandgap (~7.8 eV for MgO) of Mg render it well-suited as a chemical stressor for inducing ferroelectricity in ZnO. Additionally, comparably wider bandgap of MgO boosts the overall bandgap of Zn<sub>1-x</sub>Mg<sub>x</sub>O alloy, preventing dielectric breakdown when subjected to relatively higher magnitude electric fields. Furthermore, as Mg assumes a centrosymmetric structure, it would further stabilize the intermediate phase during phase transition and the local strain fluctuations associated with the presence of Mg dopants act to promote ferroelectric switching. A recent experimental study demonstrates ferroelectricity in Mgsubstituted ZnO thin films with the wurtzite structure [48]. Zn<sub>1-x</sub>Mg<sub>x</sub>O thin films with thicknesses of 500 nm are prepared on (111)-Pt//(0001)-Al<sub>2</sub>O<sub>3</sub> substrates at temperatures ranging from 26 to 200 °C for compositions spanning from x = 0 to x = 0.37. Their findings show that films 0.3 < x < 0.30.37, thin films display ferroelectric switching with remanent polarizations exceeding 100 μC/cm<sup>2</sup> and coercive fields below 3 MV/cm. Below this range, dielectric breakdown happens before

switching, and above this range, phase separation occurs due to high Mg content. Another study has reported a remanent polarization of  $80 \,\mu\text{C/cm}^2$  for  $\text{Zn}_{1-x}\text{Mg}_x\text{O}$  thin films [49].

While experimental results have provided significant insights, a comprehensive understanding of Zn<sub>1-x</sub>Mg<sub>x</sub>O's ferroelectric properties at an atomistic scale is crucial to harness its potential in relevant applications such as microelectronics, transducers, and photovoltaics. Density-functional theory (DFT) is often regarded as the most accurate and transferable practical model for studying the electronic structures of ferroelectric materials, as it is based on quantum-mechanical principles. However, due to its high computational demands, DFT is typically limited to relatively small length scales (~5 nm) and short time scales (<100 ps), constraining the exploration of phenomena like hysteresis loops, phase transitions, and domain wall motions that occur over larger length (~10 - 100 nm) and time scales (>ns). Force field-based methods, on the other hand, offer the computational efficiency necessary for conducting molecular dynamics (MD) simulations at length and time scales that are large enough to fully explain the complex chemistry of ferroelectric materials. Among force field-based models, the ReaxFF reactive force field [50, 51] is well suited to our problem as it can not only be utilized successfully within a single ferroelectric formulation, but also be straightforwardly extended to investigate the interactions of ferroelectric materials in multi-material interfaces, handle chemical reactions [52], and allow for studying cation substitution effects [53]. It is worth noting that Machine Learning Interatomic Potentials (MLIPs) have gained attraction in the last two decades as they have been shown to provide near-ab initio accuracy given that the high computational requirements for training stage are met [54, 55].

The aim of the current work is first to develop a ReaxFF reactive force field for  $Zn_{1-x}Mg_xO$ . Specifically, we aim to answer the question of whether doping ZnO with Mg could enable polarization reversal. Doing so would enable us to not only study ferroelectricity in Mg-substituted ZnO alloys, but also evaluate the influence of surface chemistry, point defects, Mg content and concentration, size, and scaling effects on the ferroelectric response. Using this force field, we perform MD simulations to represent the ferroelectric hysteresis loops for the  $Zn_{1-x}Mg_xO$  crystal structure. We explore the dependence of coercive field on temperature, Mg content, and Mg distribution. These findings can not only support the *Ferroelectrics Everywhere* hypothesis [48], but also motivates how tunable ferroelectric properties of  $Zn_{1-x}Mg_xO$  could be utilized in future applications.

#### 2 BACKGROUND

In this section, we discuss the previous work upon which our study is built. Specifically, we briefly explain the phase transition pathway in ZnO crystals. We then discuss developed ReaxFF reactive force fields for ZnO and MgO which we use for developing the  $Zn_{1-x}Mg_xO$  force field.

#### 2.1 Phase transition in ZnO

Zinc oxide is a transition metal oxide with the wurtzite structure as its global energy minimum under standard conditions. Four different polymorphs have been reported for ZnO. These include Wurtzite (B4), Zincblende (B1), Rocksalt (B3), and Caesium chloride (B2). Wurtzite and rocksalt structures are of particular relevance to our study as they provide the ReaxFF reactive force field with the phase transition pathway described as an asymmetric – centrosymmetric – asymmetric path. These structures are provided in Table 1 with their experimental cell parameters and bulk moduli.

Table 1. QM and ReaxFF results (at 0 K) compared to experimental data from the literature (at room temperature) for the cell axes, heats of formation ( $\Delta f$  H), bulk moduli and elastic constants of the two polymorphs (B3 and B4) of ZnO [33].

Structure	Property	B3LYP	ReaxFF	Experiment	Relative	Relative
					error	error
					(B3LYP)	(ReaxFF)
Wurtzite (B4)	a/Å	3.28	3.29	3.25	0.009	0.012
P6 <sub>3</sub> mc	c/Å	5.28	5.30	5.21	0.013	0.017
	$\Delta_{\rm f}H_{\rm B4}/({ m kcal/mol})$		-91.2	-83.3		0.095
	Bulk modulus/GPa	136	144	143	-0.049	0.007
	c <sub>11</sub> /GPa		222.9	209.7		0.063
	c <sub>12</sub> /GPa		116.3	121.1		-0.04
	c <sub>13</sub> /GPa		103.5	105.1		-0.015
	c <sub>33</sub> /GPa		212.8	210.9		0.009
	c <sub>44</sub> /GPa		57.1	42.47		0.344

Rocksalt	Bulk modulus/GPa	202	283	203	-0.005	0.394
(B3)						
Fm3m						
	a/Å	4.3	4.44	4.27	0.007	0.04
	$\Delta_{\rm f}H_{\rm B3}$ - $\Delta_{\rm f}H_{\rm B4}/({ m kcal/mol})$	37.89	37.58			

First-principles studies have identified two transition paths for wurtzite to rocksalt phase transition in ZnO [56, 57], the hexagonal and the tetragonal path. The hexagonal intermediate structure is isomorphic to the layered hexagonal boron nitride (h-BN) in which each Zn (or O) atom is located at the center of an equilateral triangle formed by three O (or Zn) atoms, and has two opposite bonds along the c axis, perpendicular to the triangle plane. The transition from wurtzite (Fig. 1(1)) to h-BN (Fig. 1 (2)) is accompanied by the compression of the axial ratio c/a from  $\sim$ 1.6 to  $\sim$ 1.2 [57]. Fig. 1 shows the phase transition pathway in ZnO under external electric field from wurtzite (Fig. 1 (1)), to h-BN (Fig. 1 (2)), back to wurtzite (Fig. 1 (3)) with opposite polarity. This transition is accompanied by a double-well energy barrier. It should be noted that the radii of atoms are adjusted for better visualization in this figure and the following figures.

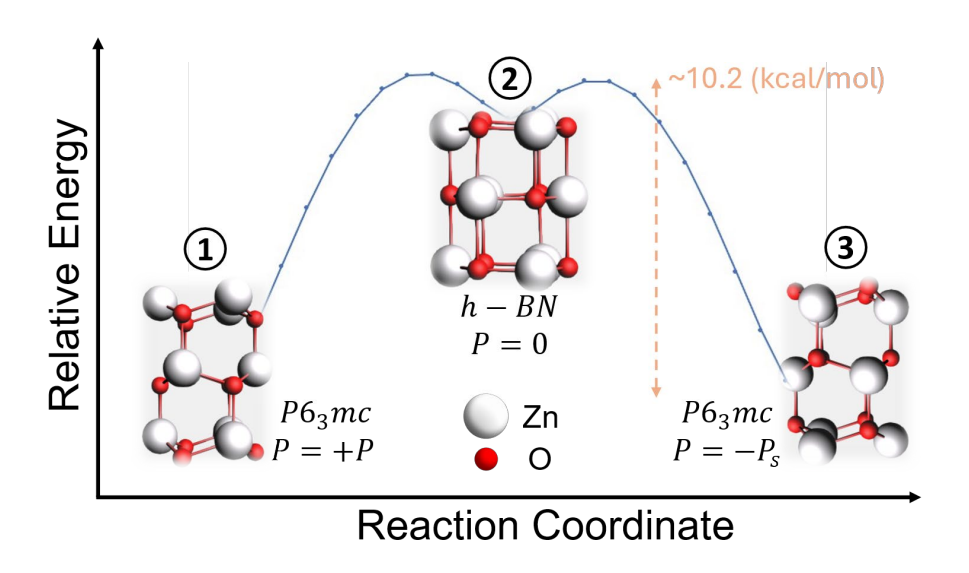


Fig. 1. Phase transition in ZnO under external electric field. The energy barrier for domain-wall migration in ZnO is approximately 10.2 kcal/mol, as shown.

## 2.2 ReaxFF reactive force fields for Zn/Mg/O

Training a ReaxFF reactive force field for Zn<sub>1-x</sub>Mg<sub>x</sub>O necessitates the inclusion of force field parameters for both ZnO and MgO. Raymand et al. [33] developed a ReaxFF reactive force field for application in MD-simulations to investigate structures and reaction dynamics for ZnO catalysts. ReaxFF parameters have been generated for Zn–O and Zn–Zn bond energies and for Zn–O–Zn, O–Zn–O, O–Zn–Zn and Zn–O–H valence angle energies. The force field has been applied in a study of the surface growth mechanism for the wurtzite [0001] surface. Cheung et al. [58] developed a ReaxFF reactive force field for Magnesium hydride systems. The parameters that were optimized for force field training against DFT data include Mg-H and Mg-Mg bond energies, and Mg-H-Mg, Mg-Mg- H, Mg-H-Mg valence angle energies. This force field has been used in MD simulations on the hydrogen absorption/desorption process in magnesium hydrides, focusing on the size effect of MgH<sub>2</sub> nanoparticles on H<sub>2</sub> desorption kinetics. Additionally, the Mg-O parameters were taken from a protein force field developed by Monti et al. [59] to study reaction mechanisms in amino acids. These two force fields form the building blocks of our force field for Zn<sub>1-x</sub>Mg<sub>x</sub>O. We initiate the force field training by merging these two force fields, as detailed in the next section.

#### 3 Methods

In this section we briefly discuss the methods we use to study ferroelectricity in  $Zn_{1-x}Mg_xO$ . These include quantum mechanical methods, ReaxFF and force field development procedure, MD simulation parameters, charge calculation methods and its limitations, and dipole analysis theory used in our analysis.

#### 3.1 First-principles methodology

The Quantum ESPRESSO [60, 61] package with norm-conserving pseudopotentials from the PseudoDojo library [62-64] were used to perform density-functional theory simulations. Electronic interactions were described using the generalized-gradient approximation [65-67] within the Perdew–Burke-Ernzerhof parametrization of the exchange-correlation potential [68]. The k-point spacing in the first Brillouin zone was set to 0.05 Å<sup>-1</sup> and the kinetic energy cutoff was set to 80 Ry with a charge density cutoff of 320 Ry. These cutoffs were chosen so that the total

energy and forces were within 1.0 meV and 25 meV per Å, respectively. The self-consistent field threshold was set to  $1.36 \times 10^{-9}$  eV. Geometry optimization of pristine ZnO and distorted Zn<sub>1-x</sub>Mg<sub>x</sub>O in the wurtzite phase was performed with total energy and force thresholds of 0.136 meV and 2.57 meV per Å, respectively.

To predict equations of state, geometry optimization of  $2 \times 2 \times 2$  supercells of  $Zn_{1-x}Mg_xO$  in the wurtzite and rocksalt phases at x = 0%, 25%, 50%, 75%, and 100% were conducted. These phases are chosen to model thermodynamic equilibrium between the end members. Zn sites for Mg substitution were chosen to minimize clustering. The total energy as a function of the lattice parameters, from 90 to 110% of the reference lattice parameters, was calculated using self-consistent field.

In the case of instrinsic (bulk) switching, geometry optimization of 3 x 3 x 2 supercells of wurtzite  $Zn_{1-x}Mg_xO$  at x = 5.6%, 11.1%, 16.7%, 22.2%, and 27.8% were conducted. Using the negatively-and positively-poled bistable states, minimum-energy pathways are calculated using the nudged-elastic-band algorithm, where a linear interpolation of images between the initial and final states was produced, and the force orthogonal to the pathway is minimized [69-71]. Seventy-five images were generated for each pathway. The self-consistent field threshold for all nudged-elastic-band simulations was reset to  $1.36 \times 10^{-5}$  eV to reduce the computational cost of the simulations while retaining sufficient accuracy.

In the case of domain-wall migration, geometry optimization of  $8 \times 1 \times 2$  supercells of wurtzite  $Zn_{1-x}Mg_xO$  at x = 12.5% were conducted such that the first and last four sets of unit cells along the crystallographic a direction are negatively- and positively-poled, respectively. The domain-wall movement is along this direction such that one set of unit cells is switched. Two cases were considered with Mg cations directly behind (B) and in front (F) of the domain wall. Twenty-five images were generated for each pathway.

#### 3.2 ReaxFF reactive force field

ReaxFF is a bond order-based [50, 72] empirical potential, which is capable of simulating bond formation and bond breaking. The total interaction energy in ReaxFF is divided into several energy

terms as shown in Eq. (3.1). Each term of the equation can derive the forces acting on each atom of the system.

$$E_{\text{system}} = E_{\text{bond}} + E_{\text{over}} + E_{\text{under}} + E_{\text{lp}} + E_{\text{val}} + E_{\text{pen}} + E_{\text{tors}} + E_{\text{conj}}$$

$$+ E_{\text{vdWaals}} + E_{\text{Coulomb}}$$
(3.1)

where E<sub>bond</sub> is bond energy, E<sub>over</sub> is over-coordination energy penalty, E<sub>under</sub> is undercoordination energy penalty, E<sub>lp</sub> is lone-pairs energy, E<sub>val</sub> is valence angle energy, E<sub>pen</sub> is energy penalty for handling double bonds, E<sub>tors</sub> is torsion angles energy, E<sub>conj</sub> is conjugated bonds energy. For handling non-bonded interactions E<sub>vdWaals</sub> aals and E<sub>Coulomb</sub> are introduced to the equation and are calculated between each atom pair, regardless of connectivity, which is different from the standard procedure in non-reactive force fields. These two terms also include a shielding parameter to avoid excessive repulsion at short distances. To eliminate any discontinuity in the non-bonded interaction energies, a seventh order Taper function is employed. A more detailed description of the terms can be found in the literature [50, 72]. All the connectivity dependent interactions such as angle and torsion terms are bond order dependent. These bond orders are calculated and updated after every iteration based on the interatomic distances. The bond order dependence ensures that each interaction's effect will smoothly go to zero during bond breaking.

We develop the ReaxFF reactive force field for  $Zn_{1-x}Mg_xO$  by initially transferring the general Zn/Mg/O parameters from existing ReaxFF reactive force fields [33]. We then tune the ReaxFF reactive force field for  $Zn_{1-x}Mg_xO$  by training against a DFT-derived training set including equations of state for wurtzite and rocksalt phases of ZnO as well as non-centrosymmetric - centrosymmetric - non-asymmetric  $Zn_{1-x}Mg_xO$  phase transition path. To reconstruct the phase transition pathway, we consider both intrinsic switching and domain wall migration mechanisms, as described in the last section. We develop the parameter set by training against available DFT data. These parameters set contains the following information:

- 1. Bond lengths for Mg-Zn, Zn-Zn, Zn-O, and Mg-O.
- 2. Bond angles for Mg-O-Zn, O-Zn-Mg, O-Mg-Zn, Zn-O-Zn, O-Zn-O, O-O-Zn, O-Zn-Zn, Mg-O-Mg, O-Mg-O, O-O-Mg, and O-Mg-Mg.
- 3. Off-diagonal terms for Zn-O and Mg-O.

The wurtzite phase in equations of states consists of a 4x2x2 super cell, whereas the rocksalt phase consists of a  $2 \times 2 \times 2$  supercell.

#### 3.3 Molecular dynamics simulations

We use our developed force field to investigate ferroelectricity in Mg-substituted ZnO across varied temperatures and Mg contents. First, we energy minimize each system, and then run energy equilibration at constant 100K NPT ensemble and using a 0.25 fs timestep. We control the temperature and pressure using Berendsen thermostats and barostats with relatively weak coupling of 100 fs, and 2500 fs, respectively. Then, we expose the system to an external electric field with a sinusoidal regime. We run the electric field simulations at temperatures of 100, 300, 500, 700, and 1000K, with various Mg contents of 0, 12.5, 18.75, 25, 31.25, and 37.5%. It should be noted that all reported percentages are molar fractions. We repeat each simulation 5 times to account for the stochasticity in evaluating the resultant coercive fields. We use the same barostat and thermostat settings in our electric field simulations as mentioned previously.

## 3.4 Charge calculation method

ReaxFF natively uses the Electron Equilibrium Method (EEM) for charge calculation. Early in our simulations we faced a limitation utilizing this method. Since EEM allows for long-distance charge transfer, our initial simulations indicated a charge transfer between top and bottom surfaces of the slab when exposed to external electric field. Such a phenomena virtually assumes conductivity in our semiconductor ZnO. As a result, a counter field would form in the bulk, preventing the ferroelectric switching when it is expected. This is illustrated in Fig. 2.

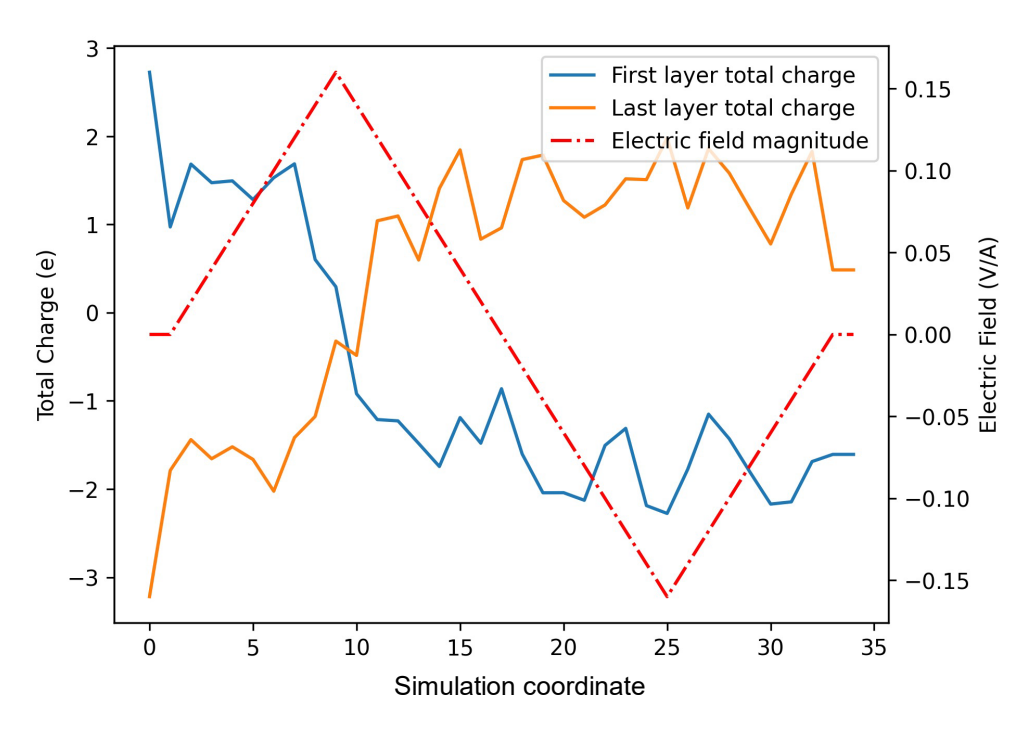


Fig. 2. The illustration of distant charge transfer between top and bottom surfaces while using EEM charge calculation method.

As shown in this figure, at the maximum positive electric field magnitude, there is a charge transfer between the top and bottom surfaces. Moreover, when the applied electric field is positive, a negative counter field is formed in the bottom layer, whereas when the applied electric field is negative, a positive counter field is formed, partially negating the electric field effects. To prevent this issue, we use the fix charge capability of ReaxFF. Specifically, after energy equilibration, we calculate the average charges of all cations (Mg, Zn) and Oxygen anions, and fix each ion's charge prior to initiating the electric field simulation. Doing so successfully prevents the charge transfer, allowing for ferroelectric switching in the absence of the artificial counter field. Our analyses show that cations typically have a positive charge of about 1, with Mg cations having slightly higher charge than Zn atoms. The same trend applies to Oxygen anions: with a typical charge of around -1, those bonded to Mg atoms have a slightly higher absolute charge value.

## 3.5 Dipole analysis and Mg spatial distribution

We calculate the total polarization of the  $Zn_{1-x}Mg_xO$  slabs using Eq. 3.2:

$$\vec{P}_{u}(t) = \frac{1}{V_{u}} \left( \sum Z_{Zn} \vec{r}_{Zn} + \sum Z_{Mg} \vec{r}_{Mg} + \sum Z_{O} \vec{r}_{O} \right)$$
(3.2)

The equation multiplies each ion's coordinate vector,  $\vec{r}_i$ , by its charge,  $Z_i$ , and divides the overall summation by the total volume of the system,  $V_u$ . The hysteresis diagrams are then drawn as P-E curves.

To investigate the effect of Mg spatial distribution on the ferroelectric properties of  $Zn_{1-x}Mg_xO$ , we consider three cases: random Mg distribution, uniform Mg distribution, and clustered Mg distribution. In random configuration, we prepare  $Zn_{1-x}Mg_xO$  slabs by randomly replacing Zn atoms with Mg atoms to the desired Mg percentage. The random placement is done using a random

number generator in Python. For uniform Mg distribution we use the *farthest point sampling* algorithm to achieve our goal. The explanation of this algorithm is as follows:

- i. Start with a system of N Zn-atoms. The goal is to replace S Zn-atoms with Mg, such that  $\frac{S}{N}$  equals the desired Mg percentage. Assume two sets which are denoted as *sampled* and *remaining* and choose a point based on steps 2 and 3.
- ii. For each point in *remaining* set, find its nearest neighbor in the *sampled set*, saving the distance.
- iii. Select the point in the *remaining* set whose nearest neighbor distance is the largest and move it from *remaining* set to *sampled*.

We use the same procedure for creating clustered Mg distribution, except that we select the smallest distance in step iii. Fig. 3 shows the resulting samples of the three distribution settings:

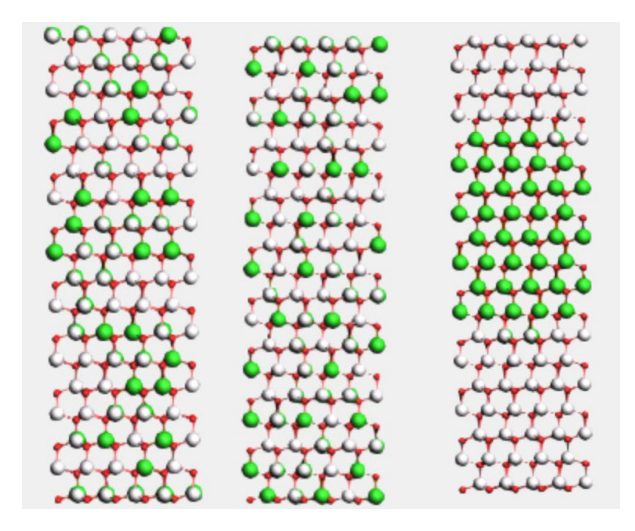


Fig. 3. Three distribution settings for Mg substitution- XZ plane view; Left: Random, middle: uniform, right: clustered. Silver, green, and red colors represent Zn, Mg, and O atoms, respectively.

#### 4 RESULTS AND DISCUSSION

## 4.1 Force field development

Fig. 4 compares the ReaxFF and DFT results for volume/energy equations of state for ferroelectric and non-ferroelectric  $Zn_{1-x}Mg_xO$  phases indicating that ReaxFF values are in consistent agreement with the calculated DFT values. The largest deviations in ReaxFF's estimation of DFT calculations are associated to endpoints where the super cell is either heavily compressed (90% of relaxed

volume) or heavily expanded (110% of the relaxed volume). It is evident from this figure that with increasing Mg%,  $Zn_{1-x}Mg_xO$  appears more stable in the rocksalt phase than the wurtzite phase. ReaxFF achieves an overall accuracy of  $R^2 = 0.96$  compared to DFT reference values.

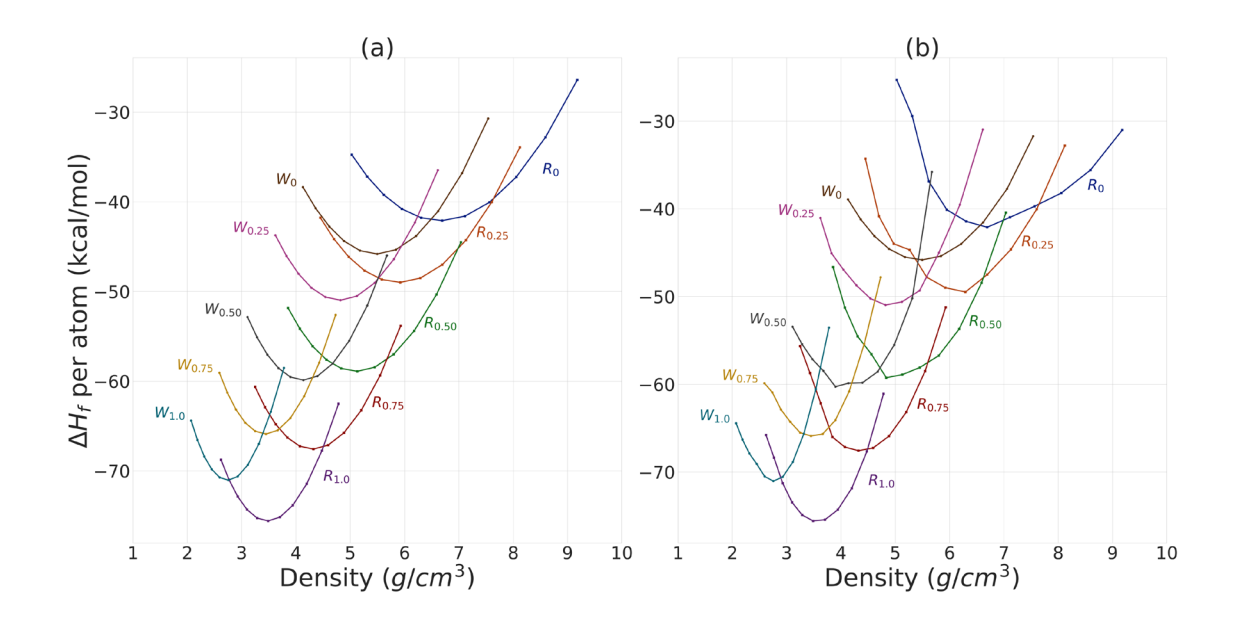


Fig. 4. Equations of state (compression/expansion) for wurtzite and rocksalt phases of  $Zn_{1-x}Mg_xO$ : a) DFT results, b) ReaxFF results; Each letter indicates the associated  $Zn_{1-x}Mg_xO$  phase as either wurtzite (W) or rocksalt (R), and each number indicates x in  $Zn_{1-x}Mg_xO$ .

We then train our force field against two switching mechanisms; in intrinsic switching, all unit cells go through phase transition at once, while in domain-wall migration, the migration of the domain-wall propagates the phase transition such that the unit cells on the opposite sides of the domain-wall have opposite polarity. DFT calculations for intrinsic switching has been carried out for Mg contents of 5.6, 11.1, 16.7, 22.2, and 27.8%. In the case of domain-wall migration, we consider the case where Mg atoms are located behind the domain-wall (denoted as B) and where Mg atoms are located at the front of the domain-wall (denoted as F). As shown in Fig. 5, ReaxFF predictions are in consistent agreement with their corresponding DFT values.  $\bar{Z}$  is the average distance of the domain-wall from the farthest layer and increasing  $\bar{Z}$  indicates the migration of the domain-wall to the opposite direction.

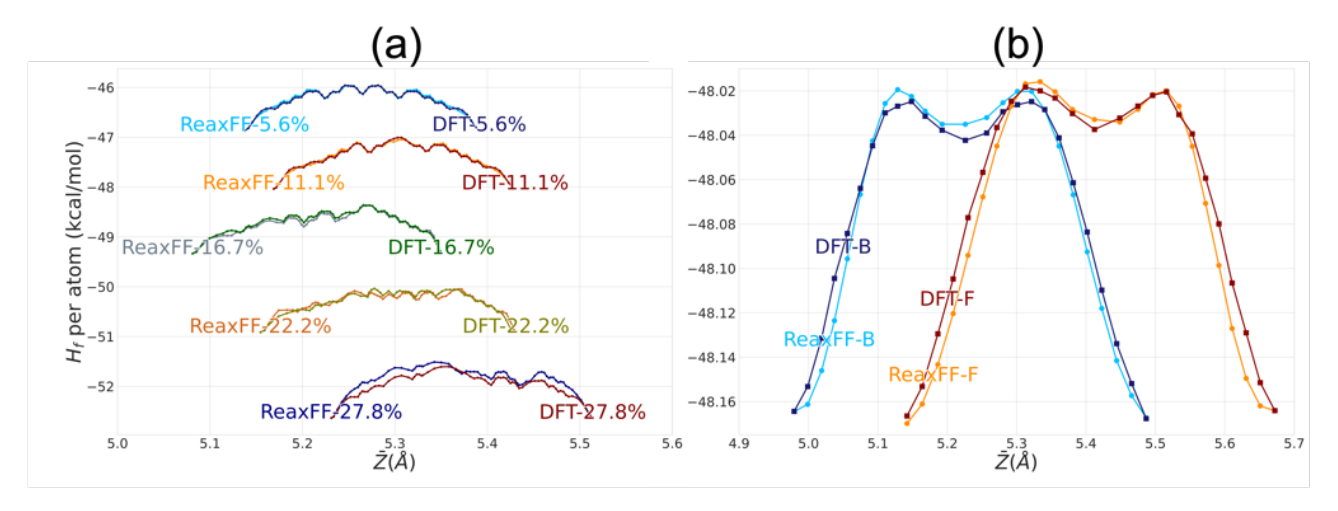


Fig 5. Energy barriers for ferroelectric switching of  $Zn_{1-x}Mg_xO$ : a) intrinsic switching, b) domain-wall migration.

Comparing the energy barriers for the two switching mechanisms, it is observed that while the barrier for intrinsic switching is 1 kcal/mol on average, the barrier for domain-wall migration is significantly smaller ( $\sim 0.15$  kcal/mol), which indicates that the desired switching mechanism is domain-wall migration. All force field parameters and Zn<sub>1-x</sub>Mg<sub>x</sub>O structure files are available in the supporting information section.

#### 4.2 MD simulations

Fig. 6 shows an overview of an electric field simulation results. In Fig. 6a, the energy curve and the applied external electric field are shown. The simulation starts with a slab of poled-up unit cells, and every sharp drop in the energy curve pinpoints the occurrence of ferroelectric switching, as shown in the inset. Observing the trajectory indicates the migration of the domain-wall from the top to the bottom layer in the presence of positive electric field, and from the bottom to the top layer in case of a negative electric field. Fig. 6b shows the results of dipole analysis, i.e., the hysteresis diagram. Our results indicate that a minimum slab thickness of ~10 nm is required to achieve a viable non-linear P-E curve. To illustrate, the hysteresis for a 7 nm slab is shown in Fig. 7b which depicts the linear P-E curve for that thickness. In smaller thicknesses, the P-E curve is either linear, or heavily distorted which could be associated to the large surface-to-bulk ratio in such thin systems. Although scale and size effects have been identified to influence hysteresis behavior [73], a comprehensive discussion on the topic is outside the scope of this manuscript and would be an objective for future research. We should note that in all our simulations, scale and size

parameters have been controlled to avoid unwanted interference when making comparisons. Fig. 6c shows the presence of 180-degree domain-wall during the polarization reversal. The domain-wall assumes a h-BN phase while the unit cells on the opposite sides of the domain-wall assume wurtzite of opposite polarity.

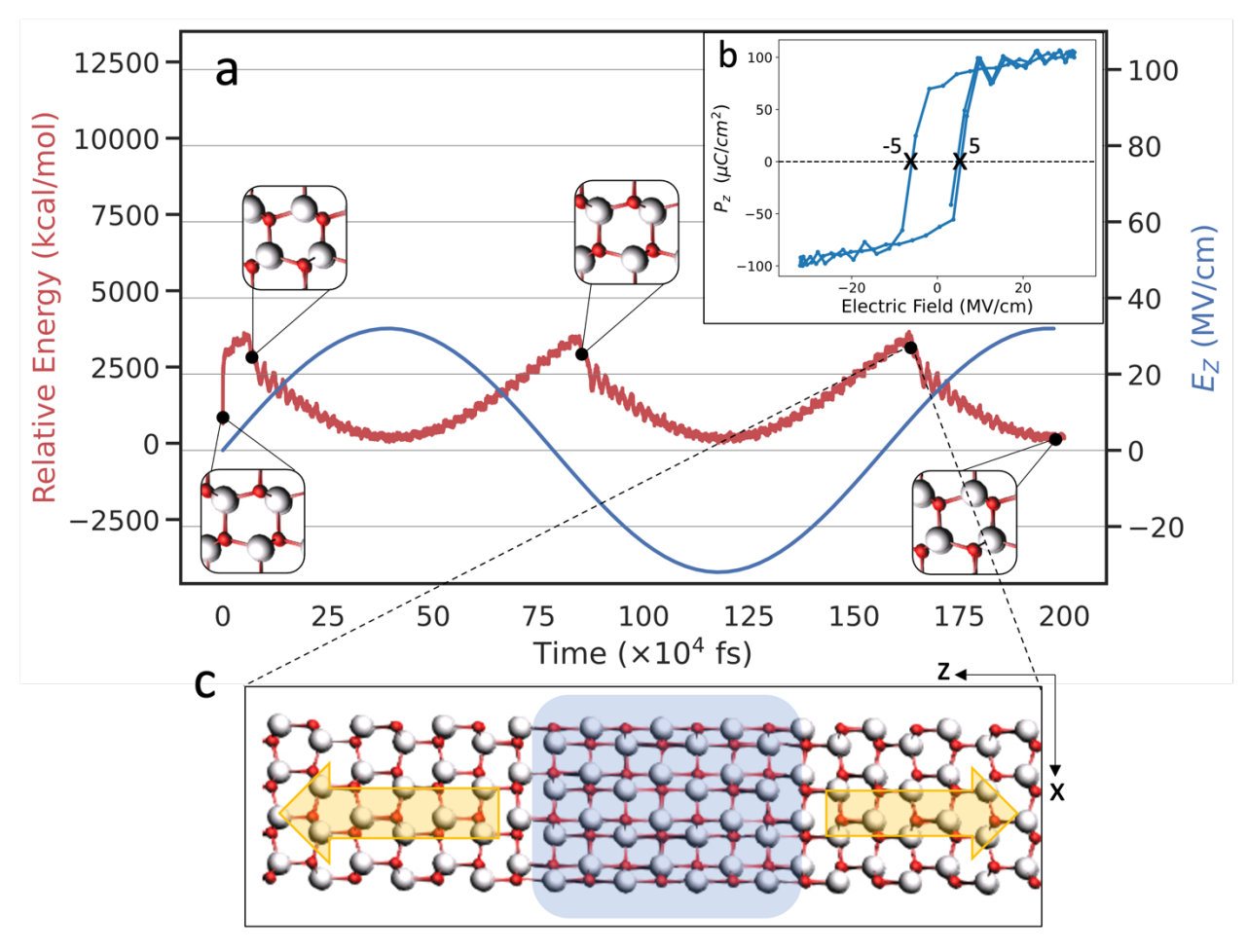


Fig 6. Electric field simulation results: a) Energy (red) and electric field (blue) vs. time with polarization reversal shown in the inset; b) P-E curve; c) Presence of 180-degree domain wall (blue) with unit cells of opposite polarities on opposing sides; arrows show the direction of the overall dipole moment in each side. The silver and red colors represent Zn and O atoms, respectively.

## 4.3 Dipole analysis

We calculate the hysteresis curves for  $Zn_{1-x}Mg_xO$  slabs of varied temperature and Mg percentage. Fig. 7 shows the results from these simulations. We run an electric field simulation on a 14 nm pure ZnO slab with a setup described earlier. The results indicate a remanent polarization of ~100  $\mu$ C/cm<sup>2</sup>. This remanent polarization is in agreement with experimental findings [48]. Additionally,

this figure shows a steady decrease in coercive field with increasing temperature, with 100 K having the maximum coercive field and 1000 K having the minimum coercive field.

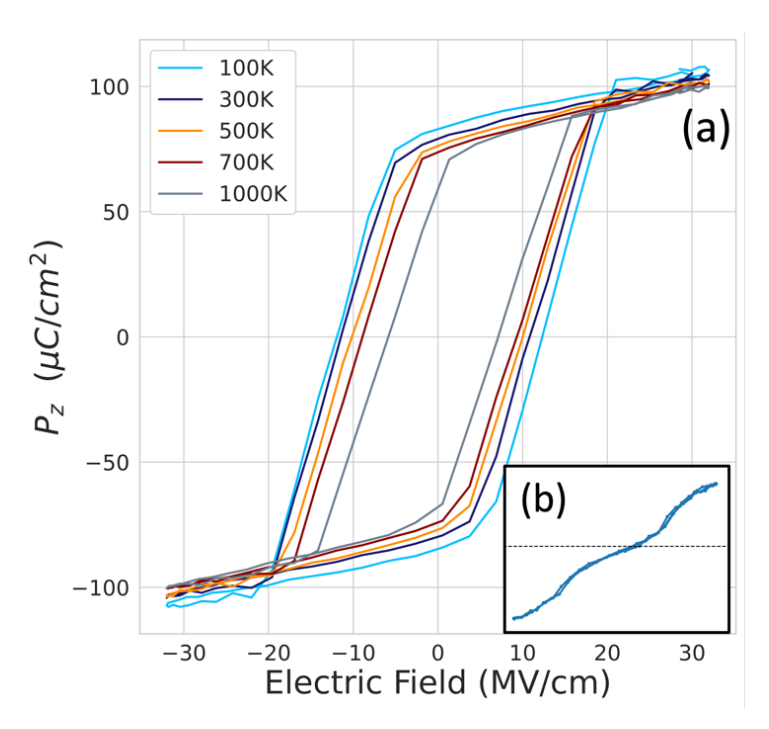


Fig 7. a) Electric field hysteresis for ZnO as a function of temperature; b) The linear P-E curve for a thickness smaller than 10 nm.

We run each simulation 5 times to account for stochasticity of ferroelectric properties each system represents. We run a total of 150 MD simulations on  $Zn_{1-x}Mg_xO$  slabs of 14nm thickness Fig. 8). The results in Fig. 8 show that the coercive field in  $Zn_{1-x}Mg_xO$  has a strong dependence to the temperature, i.e., the coercive field values drop with increasing temperature. These findings agree with the recent findings reported by Jacques et al. on studying the temperature dependence of ferroelectric switching in  $Zn_{1-x}Mg_xO$  [49].

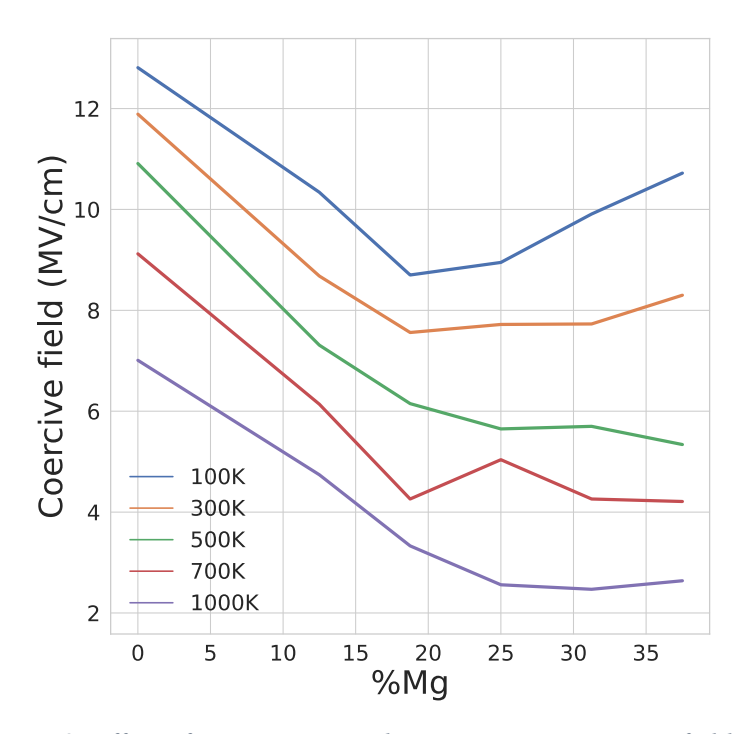


Fig 8. Effect of temperature and Mg content on coercive field.

## 4.4 Effect of Mg distribution

To investigate the effect of Mg-clustering, we create  $Zn_{1-x}Mg_xO$  slabs of 14 nm thickness and 31.25% Mg content, with three different configurations of uniform, random, and clustered Mg, as described before. We run our simulations on varied temperatures of 100, 300, 500, 700, and 1000K, to account for temperature dependence of coercive field. Fig. 9 show the results of the dipole analysis. When Mg atoms are clustered (e.g., see Fig. 3), the MgO-dominant region prefers h-BN phase, whereas ZnO-dominant regions assume wurtzite.

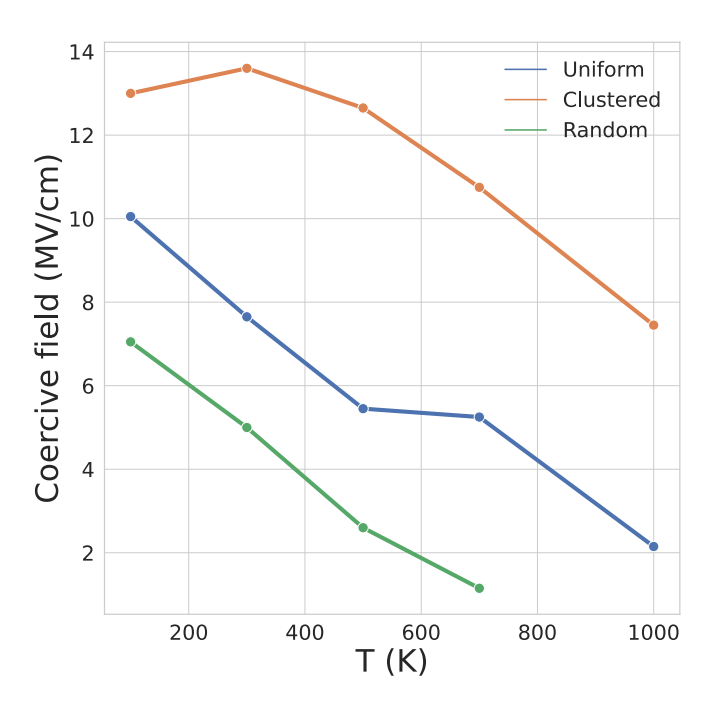


Fig 9. Coercive field as a function of Mg distribution and temperature.

Fig. 9 shows that a clustered distribution of Mg atoms results in a significant increase in the coercive field compared to an uniform or random Mg-distribution. Our simulations show that while applying an external electric field, the Mg-dominant region transitions to h-BN sooner than other regions, but transitions back to wurtzite latest. This very different behavior than observed for a slab of uniformly distributed Mg atoms where the direction of the applied electric field determines the direction of the domain-wall migration. In other words, in a clustered Mg distribution, the Mg-rich region transitions to h-BN before all other unit cells in the slab but shows a resistance upon switching back to wurtzite with opposite polarity, resulting in a delayed transition. When its neighboring ZnO-rich regions switch back, they drag the region along towards transitioning to the wurtzite phase with opposite polarity. Moreover, Fig. 9 shows a decrease in the coercive field values when Mg atoms are distributed randomly compared to a uniform distribution. The reason for this observation is unclear, however, the trend shows the presence of a minimum on coercive field between the two sides of the distribution spectrum (i.e., uniform, and clustered). More research is required to understand the reason why a deviation from a uniform distribution could result in lowered coercive fields. In a random Mg distribution, the coercive field reaches a minimum of 1.15 MV/cm at T=700K. Above this temperature, the material loses its ferroelectric behavior and presents a near-linear P-E relationship.

#### 5 CONCLUSION

We have developed a ReaxFF reactive force field for Zn<sub>1-x</sub>Mg<sub>x</sub>O by merging available force fields that include Mg-O and Zn-O parameters and further training this force field by optimizing its parameters from density-functional theory (DFT) data for equations of state and ferroelectric switching mechanisms. Our simulations show that the coercive field in Zn<sub>1-x</sub>Mg<sub>x</sub>O demonstrates a strong temperature dependence, with values decreasing as temperature increases. Interestingly, we find that the distribution of Mg atoms plays an important role in this behavior. We observe that a clustered distribution of Mg atoms results in a significant increase in the coercive field compared to uniform or random Mg-distributions, a finding that could have implications for the design of future ferroelectric materials. The reason for the observed decrease in coercive field values when Mg atoms are distributed randomly compared to a uniform distribution remains unclear, necessitating further research. The coercive field values for a random Mg distribution achieves a minimum of 1.15 MV/cm for a 31.25% Mg-substituted ZnO slab with 14.1 nm thickness. Our study contributes to the understanding of ferroelectricity in non-traditional ferroelectric materials and paves the way for the development of novel ferroelectric materials with tunable properties. The future work of this research includes the study of size and scaling effects on coercive field, the effect of surface chemistry and point defects (e.g., oxygen vacancies) on ferroelectric properties of Zn<sub>1-x</sub>Mg<sub>x</sub>O, understanding and quantification of the temperature dependence of coercive field in Zn<sub>1-x</sub>Mg<sub>x</sub>O, and optimizing Mg distribution for minimized coercive field.

#### 6 SUPPORTING INFORMATION DESCRIPTION

The force field developed in this study as well as all  $Zn_{1-x}Mg_xO$  structure files used in force field training has been provided as the supporting information.

#### 7 ACKNOWLEDGEMENT

Our work was supported as part of the center for 3D Ferroelectric Microelectronics (3DFeM), an Energy Frontier Research Center funded by the U.S. Department of Energy (DOE), Office of Science, Basic Energy Sciences under Award Number DE-SC0021118, for the new materials development. A.S. and A.C.T.v.D. also acknowledge funding from AFOSR MURI contract no. FA9550-19-1-0008.

## References

- 1. Hooker, M.W., Properties of PZT-based piezoelectric ceramics between-150 and 250 C. 1998.
- 2. Yusoff, N.H., R.A.M. Osman, M.S. Idris, K.N.D.K. Muhsen, and N.I.M. Nor. *Dielectric* and structural analysis of hexagonal and tetragonal phase BaTiO3. in AIP Conference *Proceedings*. 2020. AIP Publishing.
- 3. Hahnloser, R.H., R. Sarpeshkar, M.A. Mahowald, R.J. Douglas, and H.S. Seung, *Digital selection and analogue amplification coexist in a cortex-inspired silicon circuit.* nature, 2000. **405**(6789): p. 947-951.
- 4. Kim, J.Y., M.-J. Choi, and H.W. Jang, Ferroelectric field effect transistors: Progress and perspective. APL Materials, 2021. 9(2): p. 021102.
- 5. Merolla, P.A., J.V. Arthur, R. Alvarez-Icaza, A.S. Cassidy, J. Sawada, F. Akopyan, B.L. Jackson, N. Imam, C. Guo, and Y. Nakamura, *A million spiking-neuron integrated circuit with a scalable communication network and interface.* Science, 2014. **345**(6197): p. 668-673.
- 6. Park, Y., M.-K. Kim, and J.-S. Lee, *Emerging memory devices for artificial synapses*. Journal of Materials Chemistry C, 2020. **8**(27): p. 9163-9183.
- 7. Sun, Y., T. Karaki, and Y. Yamashita, *Recent progress on AC poling of relaxor-PbTiO3 ferroelectric single crystals: a review.* Japanese Journal of Applied Physics, 2022. **61**(SB): p. SB0802.
- 8. Zhang, H., T. Wei, Q. Zhang, W. Ma, P. Fan, D. Salamon, S.-T. Zhang, B. Nan, H. Tan, and Z.-G. Ye, *A review on the development of lead-free ferroelectric energy-storage ceramics and multilayer capacitors*. Journal of Materials Chemistry C, 2020. **8**(47): p. 16648-16667.
- 9. Han, X., Y. Ji, and Y. Yang, *Ferroelectric photovoltaic materials and devices*. Advanced Functional Materials, 2022. **32**(14): p. 2109625.
- 10. Ma, T. and J.-P. Han, *Why is nonvolatile ferroelectric memory field-effect transistor still elusive?* IEEE Electron Device Letters, 2002. **23**(7): p. 386-388.
- 11. Kohlstedt, H., Y. Mustafa, A. Gerber, A. Petraru, M. Fitsilis, R. Meyer, U. Böttger, and R. Waser, *Current status and challenges of ferroelectric memory devices*. Microelectronic Engineering, 2005. **80**: p. 296-304.
- 12. Borkar, H., V. Singh, B. Singh, M. Tomar, V. Gupta, and A. Kumar, *Room temperature lead-free relaxor–antiferroelectric electroceramics for energy storage applications*. RSC Advances, 2014. **4**(44): p. 22840-22847.
- 13. Li, W.-B., D. Zhou, and L.-X. Pang, *Enhanced energy storage density by inducing defect dipoles in lead free relaxor ferroelectric BaTiO3-based ceramics*. Applied Physics Letters, 2017. **110**(13): p. 132902.
- 14. Qu, B., H. Du, and Z. Yang, *Lead-free relaxor ferroelectric ceramics with high optical transparency and energy storage ability.* Journal of Materials Chemistry C, 2016. **4**(9): p. 1795-1803.
- 15. Yang, C.-H., J. Seidel, S. Kim, P. Rossen, P. Yu, M. Gajek, Y.-H. Chu, L.W. Martin, M. Holcomb, and Q. He, *Electric modulation of conduction in multiferroic Ca-doped BiFeO3 films*. Nature materials, 2009. **8**(6): p. 485-493.
- 16. Shi, T., G. Li, and J. Zhu, *Compositional design strategy for high performance ferroelectric oxides with perovskite structure*. Ceramics International, 2017. **43**(3): p. 2910-2917.

- 17. Limpichaipanit, A. and A. Ngamjarurojana, Effect of Li and Bi co-doping and sintering temperature on dielectric properties of PLZT 9/65/35 ceramics. Ceramics International, 2017. 43(5): p. 4450-4455.
- 18. Jung, Y.-S., E.-S. Na, U. Paik, J. Lee, and J. Kim, *A study on the phase transition and characteristics of rare earth elements doped BaTiO3*. Materials research bulletin, 2002. **37**(9): p. 1633-1640.
- 19. Yasmm, S., S. Choudhury, M. Hakim, A. Bhuiyan, and M. Rahman, *Effect of cerium doping on microstructure and dielectric properties of BaTiO3 ceramics*. Journal of Materials Science & Technology, 2011. **27**(8): p. 759-763.
- 20. West, A.R., T.B. Adams, F.D. Morrison, and D.C. Sinclair, *Novel high capacitance materials:-BaTiO3: La and CaCu3Ti4O12*. Journal of the European Ceramic Society, 2004. **24**(6): p. 1439-1448.
- 21. Khirade, P.P., S.D. Birajdar, A. Raut, and K. Jadhav, *Multiferroic iron doped BaTiO3* nanoceramics synthesized by sol-gel auto combustion: influence of iron on physical properties. Ceramics International, 2016. **42**(10): p. 12441-12451.
- 22. Haertling, G.H., *Ferroelectric ceramics: history and technology.* Journal of the American Ceramic Society, 1999. **82**(4): p. 797-818.
- 23. Chen, W., X. Zhao, J. Sun, L. Zhang, and L. Zhong, *Effect of the Mn doping concentration on the dielectric and ferroelectric properties of different-routes-fabricated BaTiO3-based ceramics*. Journal of Alloys and Compounds, 2016. **670**: p. 48-54.
- 24. Von Hippel, A., *Piezoelectricity, ferroelectricity, and crystal structure*. Zeitschrift für Physik A Hadrons and nuclei, 1952. **133**: p. 158-173.
- 25. Megaw, H.D., Ferroelectricity in crystals. 1957: Methuen.
- 26. Burns, G., Solid State Physics Academic Press Inc. New York, 1985.
- 27. Müller, J., U. Schröder, T. Böscke, I. Müller, U. Böttger, L. Wilde, J. Sundqvist, M. Lemberger, P. Kücher, and T. Mikolajick, *Ferroelectricity in yttrium-doped hafnium oxide*. Journal of Applied Physics, 2011. **110**(11): p. 114113.
- 28. Fichtner, S., N. Wolff, F. Lofink, L. Kienle, and B. Wagner, *AlScN: A III-V semiconductor based ferroelectric*. Journal of Applied Physics, 2019. **125**(11): p. 114103.
- 29. Moriwake, H., A. Konishi, T. Ogawa, K. Fujimura, C.A. Fisher, A. Kuwabara, T. Shimizu, S. Yasui, and M. Itoh, *Ferroelectricity in wurtzite structure simple chalcogenide*. Applied Physics Letters, 2014. **104**(24): p. 242909.
- 30. Albertsson, J., S. Abrahams, and Å. Kvick, *Atomic displacement, anharmonic thermal vibration, expansivity and pyroelectric coefficient thermal dependences in ZnO*. Acta Crystallographica Section B: Structural Science, 1989. **45**(1): p. 34-40.
- 31. Tsukazaki, A., A. Ohtomo, T. Onuma, M. Ohtani, T. Makino, M. Sumiya, K. Ohtani, S.F. Chichibu, S. Fuke, and Y. Segawa, *Repeated temperature modulation epitaxy for p-type doping and light-emitting diode based on ZnO*. Nature materials, 2005. **4**(1): p. 42-46.
- 32. Repins, I., M.A. Contreras, B. Egaas, C. DeHart, J. Scharf, C.L. Perkins, B. To, and R. Noufi, 19· 9%-efficient ZnO/CdS/CuInGaSe2 solar cell with 81· 2% fill factor. Progress in Photovoltaics: Research and applications, 2008. **16**(3): p. 235-239.
- 33. Raymand, D., A.C. Van Duin, M. Baudin, and K. Hermansson, *A reactive force field* (*ReaxFF*) for zinc oxide. Surface science, 2008. **602**(5): p. 1020-1031.
- 34. Pearton, S., D. Norton, K. Ip, Y. Heo, and T. Steiner, *RETRACTED: Recent progress in processing and properties of ZnO*. Progress in materials science, 2005. **50**(3): p. 293-340.

- 35. Özgür, Ü., Y.I. Alivov, C. Liu, A. Teke, M. Reshchikov, S. Doğan, V. Avrutin, S.-J. Cho, and Morkoç, *A comprehensive review of ZnO materials and devices*. Journal of applied physics, 2005. **98**(4): p. 11.
- 36. Morkoç, H. and Ü. Özgür, *Zinc oxide: fundamentals, materials and device technology.* 2008: John Wiley & Sons.
- 37. Klingshirn, C., *ZnO: From basics towards applications*. physica status solidi (b), 2007. **244**(9): p. 3027-3073.
- 38. Janotti, A. and C.G. Van de Walle, *Fundamentals of zinc oxide as a semiconductor*. Reports on progress in physics, 2009. **72**(12): p. 126501.
- 39. Guo, H., N. Lu, J. Dai, X.C. Zeng, X. Wu, and J. Yang, *Electronic structure engineering in chemically modified ultrathin ZnO nanofilms via a built-in heterointerface*. RSC Advances, 2014. **4**(36): p. 18718-18723.
- 40. Behera, H. and G. Mukhopadhyay, *Strain-tunable band parameters of ZnO monolayer in graphene-like honeycomb structure*. Physics Letters A, 2012. **376**(45): p. 3287-3289.
- 41. Ohtomo, A., M. Kawasaki, T. Koida, K. Masubuchi, H. Koinuma, Y. Sakurai, Yasuda Yoshida, T. Yasuda, and Y. Segawa., "Mg x Zn 1- x O as a II-VI widegap semiconductor alloy.". Applied physics letters 1998. **72.19 (1998): 2466-2468.**
- 42. Gruber, T., C. Kirchner, R. Kling, F. Reuss, and A. Waag, *ZnMgO epilayers and ZnO–ZnMgO quantum wells for optoelectronic applications in the blue and UV spectral region*. Applied physics letters, 2004. **84**(26): p. 5359-5361.
- 43. Minemoto, T., T. Negami, S. Nishiwaki, H. Takakura, and Y. Hamakawa, *Preparation of Zn1-xMgxO films by radio frequency magnetron sputtering*. Thin solid films, 2000. **372**(1-2): p. 173-176.
- 44. Kumar, P., H.K. Malik, A. Ghosh, R. Thangavel, and K. Asokan, *Bandgap tuning in highly c-axis oriented Zn1-xMgxO thin films*. Applied Physics Letters, 2013. **102**(22): p. 221903.
- 45. Koike, K., K. Hama, I. Nakashima, G.-y. Takada, K.-i. Ogata, S. Sasa, M. Inoue, and M. Yano, *Molecular beam epitaxial growth of wide bandgap ZnMgO alloy films on (1 1 1)-oriented Si substrate toward UV-detector applications*. Journal of crystal growth, 2005. **278**(1-4): p. 288-292.
- 46. Kang, X., S. Shetty, L. Garten, J.F. Ihlefeld, S. Trolier-McKinstry, and J.-P. Maria, Enhanced dielectric and piezoelectric responses in Zn1-x Mg x O thin films near the phase separation boundary. Applied Physics Letters, 2017. 110(4): p. 042903.
- 47. Konishi, A., T. Ogawa, C.A. Fisher, A. Kuwabara, T. Shimizu, S. Yasui, M. Itoh, and H. Moriwake, *Mechanism of polarization switching in wurtzite-structured zinc oxide thin films*. Applied Physics Letters, 2016. **109**(10).
- 48. Ferri, K., S. Bachu, W. Zhu, M. Imperatore, J. Hayden, N. Alem, N. Giebink, S. Trolier-McKinstry, and J.-P. Maria, *Ferroelectrics everywhere: Ferroelectricity in magnesium substituted zinc oxide thin films.* Journal of Applied Physics, 2021. **130**(4): p. 044101.
- 49. Jacques, L., G. Ryu, D. Goodling, S. Bachu, R. Taheri, P. Yousefian, S. Shetty, B. Akkopru-Akgun, C. Randall, and N. Alem, *Wake up and retention in zinc magnesium oxide ferroelectric films*. Journal of Applied Physics, 2023. **133**(22): p. 224102.
- 50. Van Duin, A.C., S. Dasgupta, F. Lorant, and W.A. Goddard, *ReaxFF: a reactive force field for hydrocarbons*. The Journal of Physical Chemistry A, 2001. **105**(41): p. 9396-9409.
- 51. Chenoweth, K., A.C. Van Duin, and W.A. Goddard, *ReaxFF reactive force field for molecular dynamics simulations of hydrocarbon oxidation*. The Journal of Physical Chemistry A, 2008. **112**(5): p. 1040-1053.

- 52. Akbarian, D., D.E. Yilmaz, Y. Cao, P. Ganesh, I. Dabo, J. Munro, R. Van Ginhoven, and A.C. Van Duin, *Understanding the influence of defects and surface chemistry on ferroelectric switching: a ReaxFF investigation of BaTiO 3*. Physical Chemistry Chemical Physics, 2019. **21**(33): p. 18240-18249.
- 53. Akbarian, D., N. Nayir, and A.C. Van Duin, *Understanding physical chemistry of Ba x Sr 1-x TiO 3 using ReaxFF molecular dynamics simulations*. Physical Chemistry Chemical Physics, 2021. **23**(44): p. 25056-25062.
- 54. Mortazavi, B., B. Javvaji, F. Shojaei, T. Rabczuk, A.V. Shapeev, and X. Zhuang, *Exceptional piezoelectricity, high thermal conductivity and stiffness and promising photocatalysis in two-dimensional MoSi2N4 family confirmed by first-principles.* Nano Energy, 2021. **82**: p. 105716.
- 55. Ko, T.W. and S.P. Ong, *Recent advances and outstanding challenges for machine learning interatomic potentials*. Nature Computational Science, 2023. **3**(12): p. 998-1000.
- 56. Saitta, A.M. and F. Decremps, *Unifying description of the wurtzite-to-rocksalt phase transition in wide-gap semiconductors: The effect of d electrons on the elastic constants.* Physical Review B, 2004. **70**(3): p. 035214.
- 57. Cai, J. and N. Chen, *First-principles study of the wurtzite-to-rocksalt phase transition in zinc oxide*. Journal of Physics: Condensed Matter, 2007. **19**(26): p. 266207.
- 58. Cheung, S., W.-Q. Deng, A.C. Van Duin, and W.A. Goddard, *ReaxFFMgH reactive force field for magnesium hydride systems*. The Journal of Physical Chemistry A, 2005. **109**(5): p. 851-859.
- 59. Monti, S., A. Corozzi, P. Fristrup, K.L. Joshi, Y.K. Shin, P. Oelschlaeger, A.C. Van Duin, and V. Barone, *Exploring the conformational and reactive dynamics of biomolecules in solution using an extended version of the glycine reactive force field.* Physical Chemistry Chemical Physics, 2013. **15**(36): p. 15062-15077.
- 60. Giannozzi, P., S. Baroni, N. Bonini, M. Calandra, R. Car, C. Cavazzoni, D. Ceresoli, G.L. Chiarotti, M. Cococcioni, and I. Dabo, *QUANTUM ESPRESSO: a modular and open-source software project for quantum simulations of materials.* Journal of physics: Condensed matter, 2009. **21**(39): p. 395502.
- 61. Giannozzi, P., O. Andreussi, T. Brumme, O. Bunau, M.B. Nardelli, M. Calandra, R. Car, C. Cavazzoni, D. Ceresoli, and M. Cococcioni, *Advanced capabilities for materials modelling with Quantum ESPRESSO*. Journal of physics: Condensed matter, 2017. **29**(46): p. 465901.
- 62. van Setten, M.J., M. Giantomassi, E. Bousquet, M.J. Verstraete, D.R. Hamann, X. Gonze, and G.-M. Rignanese, *The PseudoDojo: Training and grading a 85 element optimized norm-conserving pseudopotential table.* Computer Physics Communications, 2018. **226**: p. 39-54.
- 63. Lejaeghere, K., G. Bihlmayer, T. Björkman, P. Blaha, S. Blügel, V. Blum, D. Caliste, I.E. Castelli, S.J. Clark, and A. Dal Corso, *Reproducibility in density functional theory calculations of solids*. Science, 2016. **351**(6280): p. aad3000.
- 64. Hamann, D., *Optimized norm-conserving Vanderbilt pseudopotentials*. Physical Review B, 2013. **88**(8): p. 085117.
- 65. Perdew, J.P., J.A. Chevary, S.H. Vosko, K.A. Jackson, M.R. Pederson, D.J. Singh, and C. Fiolhais, *Atoms, molecules, solids, and surfaces: Applications of the generalized gradient approximation for exchange and correlation.* Physical review B, 1992. **46**(11): p. 6671.

- 66. Langreth, D.C. and M. Mehl, *Beyond the local-density approximation in calculations of ground-state electronic properties.* Physical Review B, 1983. **28**(4): p. 1809.
- 67. Becke, A.D., *Density-functional exchange-energy approximation with correct asymptotic behavior.* Physical review A, 1988. **38**(6): p. 3098.
- 68. Perdew, J.P., K. Burke, and M. Ernzerhof, *Generalized gradient approximation made simple*. Physical review letters, 1996. 77(18): p. 3865.
- 69. Jónsson, H., G. Mills, and K.W. Jacobsen, *Nudged elastic band method for finding minimum energy paths of transitions*, in *Classical and quantum dynamics in condensed phase simulations*. 1998, World Scientific. p. 385-404.
- 70. Henkelman, G., B.P. Uberuaga, and H. Jónsson, *A climbing image nudged elastic band method for finding saddle points and minimum energy paths*. The Journal of chemical physics, 2000. **113**(22): p. 9901-9904.
- 71. Henkelman, G. and H. Jónsson, *Improved tangent estimate in the nudged elastic band method for finding minimum energy paths and saddle points*. The Journal of chemical physics, 2000. **113**(22): p. 9978-9985.
- 72. Van Duin, A.C., A. Strachan, S. Stewman, Q. Zhang, X. Xu, and W.A. Goddard, *ReaxFFSiO reactive force field for silicon and silicon oxide systems.* The Journal of Physical Chemistry A, 2003. **107**(19): p. 3803-3811.
- 73. Ihlefeld, J.F., D.T. Harris, R. Keech, J.L. Jones, J.P. Maria, and S. Trolier-McKinstry, Scaling effects in perovskite ferroelectrics: fundamental limits and process-structure-property relations. Journal of the American Ceramic Society, 2016. 99(8): p. 2537-2557.

# TOC GRAPHIC

